

Laser-stimulated 4D printing of magnetostrictive Fe-Co-V

Received: 23 December 2024

Accepted: 30 January 2026

Published online: 10 February 2026

Guiwei Li¹✉, Zeyu Yang, Aodu Zheng, Qi Tian, Qi Li¹✉, Xin Wang¹✉ & Wenzheng Wu✉

Magnetostrictive materials hold non-contact stimulation-responsive properties, which exhibit promising prospects in aviation and marine engineering. However, high-end equipment is frequently employed in changeable environments during service. A slight deformation in magnetostrictive effect makes it complicated to meet the demands of macroscopic applications. 4D printing is that the 3D printed object could evolve with time when it is under specific stimuli. Herein, we present a method of 4D printing magnetostrictive materials to endow service parts with laser-responsive macroscopic strain and magnetically responsive microscopic strain. The internal stress in laser powder bed fused magnetostrictive samples can be redistributed via adjusting laser stimulation parameters and scanning strategies. This redistribution induces macroscopic plastic deformation at the selected location. Dynamic control of the samples' microstructure and electromagnetic properties can be accomplished during shape-morphing stimulation. This breakthrough addresses the strain scale limitations of magnetostrictive materials, promoting the cross-scale shape-morphing application of 4D printing in electromagnetic engineering.

Magnetostrictive materials exhibit non-contact responsive magneto-mechanical energy conversion capabilities. This property endows them with irreplaceable potential in precision actuation, vibration control, and energy harvesting applications^{1–5}. Terfenol-D^{6–9}, Fe-Ga^{10–12} and Fe-Co^{13–16} alloys are representative magnetostrictive materials. These materials demonstrate favorable magnetostriction performance and high sensitivity. Additionally, they maintain excellent thermal stability. However, their large-scale industrial adoption remains constrained. This limitation primarily stems from inherent defects in conventional fabrication methods. For instance, smelting processes frequently induce compositional segregation. Powder metallurgy faces dual challenges of achieving high densification and precise grain orientation control¹⁷. Thin-film deposition techniques exhibit insufficient mechanical robustness for macroscopic device integration¹⁸. In high-performance electromagnetic systems, stringent requirements are imposed. Materials must simultaneously deliver large strain outputs and rapid dynamic responses. Structural adaptability to complex

geometries is also essential. These demands create multi-dimensional challenges for advanced manufacturing technologies.

Metal additive manufacturing technologies, particularly laser powder bed fusion (LPBF), have achieved breakthroughs in grain orientation control of magnetostrictive alloys^{19–23}. Gao et al. implemented a layer-by-layer melting-solidification strategy combined with controlled grain growth protocols, and the magnetostrictive strain of Fe₈₁Ga₁₉ alloy was enhanced to 77.2 ppm via the scanning path optimization²⁴. Riipinen et al. systematically investigated the LPBF parameter optimization for Fe-Co-V alloy fabrication, and the sample porosity was reduced to below 0.5% through process refinement. This microstructural improvement significantly enhanced the magnetic performance of printed samples²⁵. Furthermore, the post-LPBF annealing investigation revealed that Fe-Co-V alloys grain structure evolution and size modification critically influenced magnetic properties²⁶. However, current researches mainly focus on static magneto-mechanical performance enhancement. The fundamental

School of Mechanical and Aerospace Engineering, Jilin University, Changchun, Jilin, China. ✉ e-mail: ligw@jlu.edu.cn; qli22@mails.jlu.edu.cn; wxin@jlu.edu.cn; wzwwu@jlu.edu.cn

challenge of dynamic performance regulation during material service remains unaddressed. This investigation proposes a laser-assisted post-processing strategy for LPBF-fabricated metallic structures. The as-built components can be deformed with the stimulation of laser. This approach confers dynamic programmability in geometry, performance, and functionality post-fabrication.

The Fe-Co-V alloy is employed as the magnetostrictive matrix material, unlike conventional 4D printing relying on the passive thermal responses of shape memory alloys²⁷. The Fe-Co-V system exhibits a high saturation magnetostriction coefficient, and the vanadium (V) doping enhances fatigue resistance. The cyclic stability shows marked improvement compared to binary Fe-Co systems. Furthermore, the alloy maintains robust temperature stability at elevated temperatures. This characteristic enables reliable operation in extreme environments. And the magneto-elastic coupling properties of Fe-Co-V enable bidirectional energy conversion. This dual-mode conversion can be triggered by external magnetic or stress fields^{28,29}. Such intrinsic behavior establishes a physical foundation for dynamic regulation in 4D-printed systems.

Herein, we present a laser-stimulated 4D printing strategy for magnetostrictive Fe-Co-V alloy. This approach achieves integrated material-structure-function design. The experimental procedure involves two critical stages. First, the Fe-Co-V alloy components with complex architectures are fabricated via the LPBF technology. Subsequently, the gradient thermal stress fields are induced in designated regions through programmable laser scanning. The process incorporates dual regulation mechanisms. Thermal stress-induced plastic deformation enables predefined macroscopic shape transformation. Simultaneously, laser stimulation generates localized lattice distortion and magnetic domain reconstruction. These synergistic effects enhance magnetostriction performance for microscopic property modulation. This investigation introduces Fe-Co-V alloy into 4D printing systems. A magneto-thermo-mechanical coupled design framework is established. And a laser-stimulated dynamic regulation method for metallic components is proposed. The methodology achieves synchronous optimization of macroscopic deformation and microscopic magnetic properties. This breakthrough extends magnetostrictive material applications beyond conventional boundaries. It advances 4D printing from “shape programming” to “performance programming” paradigms. Critical technical foundations are established for strategic applications of aerospace electromagnetic shielding systems and marine equipment energy recovery solutions^{30,31}.

Results and discussion

The shape-morphing processes of LPBF Fe-Co-V samples are stimulated via programming the laser rescanning strategies. Figure 1a illustrates the schematic of metallic 4D printing of laser stimulation. The dark red area represents the regions stimulated by the laser to induce bending deformation, while the blue area denotes sections intentionally unstimulated. To clearly present the mechanism and process by which laser stimulation enables a prototype to achieve 4D printing deformation, Fig. 1b illustrates the macroscopic dynamic transformation. It depicts the progression from a 2D planar design to the creation of a 3D structure, followed by the targeted laser stimulation of specific regions to achieve the desired 4D printing deformation. The 2D structure is initially fabricated via the LPBF. Then, through programming the laser parameters and scanning paths on the sample's surface, the macrodynamic transformation of the laser-stimulated sample from a 2D to a 3D structure is ultimately achieved. Yellow arrows represent the impact of the laser beam on the sample, while red arrows indicate the movement direction of the laser beam. Figure 1c presents the shape-morphing processes of laser stimulation (Supplementary Movie 1). Four selected transient states were captured during the deformation process. The images demonstrate that the bending of the

sample becomes increasingly pronounced with the increasing of laser scanning times. This further provides the reliability and practicality of the Fe-Co-V 4D printing via the laser stimulation.

To analyze the effects of laser stimulation on the physical phase composition, the X-ray diffraction was employed to test the 4D-printed Fe-Co-V samples. The XRD analysis results were illustrated in Fig. 1d and Supplementary Fig. 1. It is evident that the three primary diffraction peaks correspond to CoFe. And it shows a notable reduction in the number of impurity peaks compared with the Supplementary Fig. 1. To further explore the mechanical properties of these samples, a rectangular specimen was selected for compression testing. This specimen is depicted in Fig. 1c. During the test, three instantaneous states of the deformed sample under applied force were recorded in the Supplementary Fig. 2.

The force-displacement curves of the laser-stimulated 4D printed samples under different stimulation times are shown in Fig. 1e. The maximum load that the laser-stimulated 4D printed samples can bear, based on the number of laser stimulations, is illustrated in Fig. 1f (Each mean is calculated with the testing results of five samples, while the error bars represent the standard deviation). By analyzing these curves, it can be concluded that the slope of the curve is steeper at lower laser stimulation counts. This indicates that the material exhibits higher resistance at smaller displacement. As the number of laser stimulations increases, the brown and orange curves gradually flatten. This suggests that the material requires larger displacements to exhibit greater resistance. With lower stimulation counts (2 and 4 times), the steep rise in the curves indicates that the material has strong resistance to deformation in the initial loading phase but may enter the failure stage earlier. When the laser stimulation count continues to increase, the material's ductility enhances. The experimental results presented in Fig. 1f show that the maximum load that the sample can withstand changes with the number of laser stimulations. When the laser stimulation count reaches 8, the maximum load the sample can bear reaches its peak value of 57.33 N. When the laser stimulation count reaches 10, the maximum load the sample can bear drops to its minimum value of 26.94 N. This could also be attributed to microstructural changes, such as grain growth, residual stress concentration, or crack initiation, which result in a notable decrease in sample strength. The shape-morphing degrees of the Fe-Co-V samples can be dynamically adjusted through controlling the laser stimulation times. Furthermore, the various mechanical properties of the shape-morphing samples can be obtained based on the same batch.

To clarify how laser stimulation induces property changes in 4D printing, scanning electron microscope (SEM) was utilized. Figure 1g shows the examination of the samples' microscopic surface morphology during the shape-morphing process. In comparison, the micro-surface morphology of the laser-stimulated 4D-printed sample shows significant improvement. Only slight traces of laser scanning and a few scattered globular particles are attached to the surface³². Supplementary Fig. 3 demonstrates how surface profilometry and the shape of the sample change with varying numbers of laser scans. As the number of stimulation times increases, the bending deformation of the 4D-printed sample progressively intensifies, while its surface laser scanning traces become increasingly attenuated. The surface roughness of the sample subjected to 8 laser stimulation times decreased by 61.6% compared to the LPBF sample. To further identify the composition and elemental content ratios on the sample's surface, the EDS analysis images are presented in Fig. 1h. In comparison to the EDS image of the LPBF sample surface (Supplementary Fig. 4), the 4D-printed sample shows a more organized distribution of surface elements. Additionally, there is a notable increase in O content. This could be attributed to the presence of trace amounts of oxygen in the printing chamber during laser stimulation. The oxygen likely reacts with the metal elements on the sample surface, forming oxides that adhere to the surface of the 4D-printed samples at high temperatures.

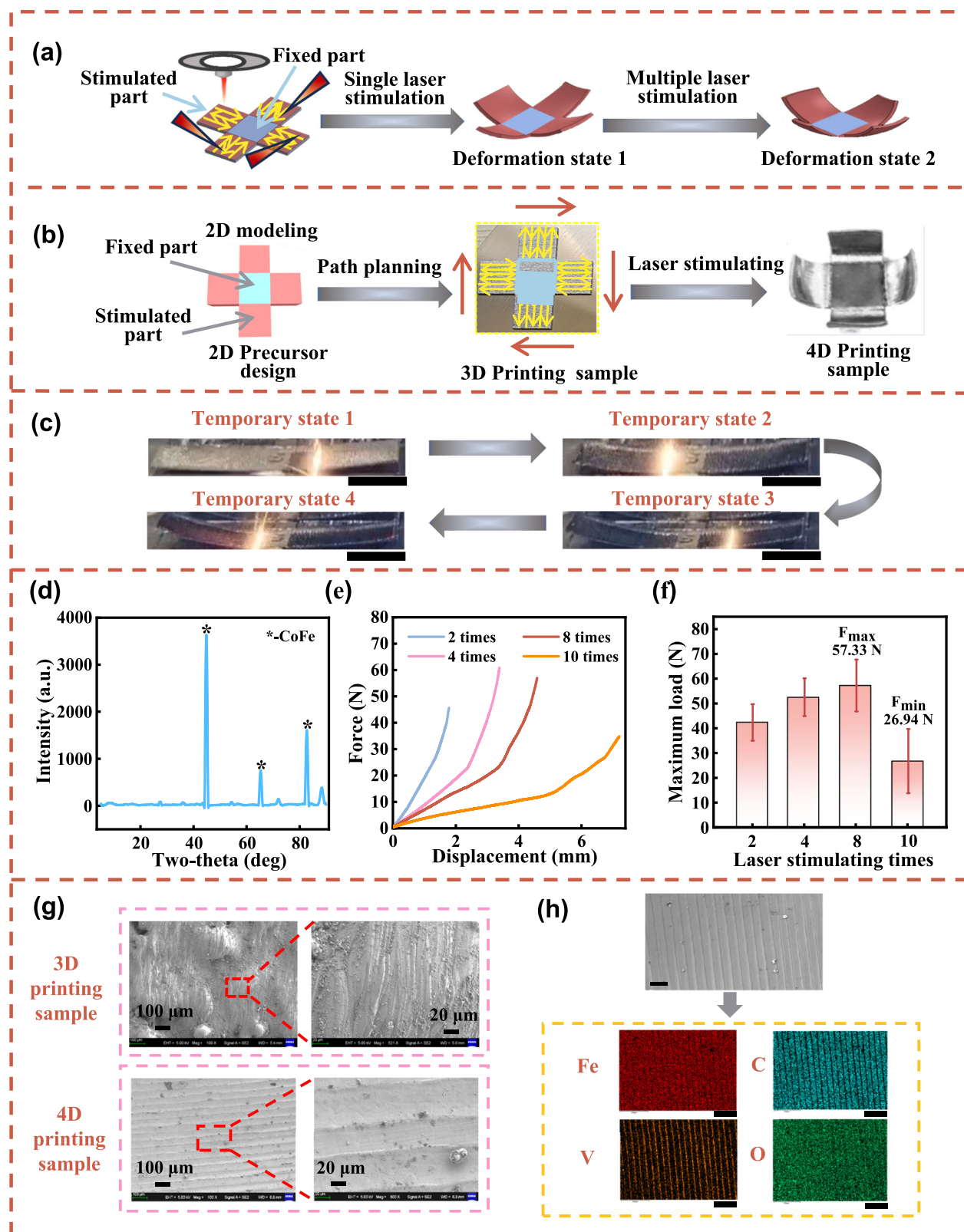


Fig. 1 | The schematic of macroscopic shape-morphing of magnetostrictive samples. **a** The deformation schematic from a planar structure to a 3D structure. **b** The sequence of steps from 2D precursor design to the creation of a LPBF sample, culminating in a 4D printed sample after laser stimulation. **c** The dynamic deformation states of a LPBF rectangular sample during laser stimulation. Scale bar:

10 mm. **d** XRD analysis of the surface of the 4D-printed sample. **e** Force-displacement curves of the 4D printed sample after laser-induced deformation. **f** Maximum load testing results for the 4D printed samples. **g** SEM images of the surface change in the 4D printing process. **h** EDS images of the 4D printed sample. Scale bar: 100 μm . (Source data are provided as a Source Data file).

The specific composition and proportions of the powder are provided in Supplementary Fig. 5 and Supplementary Table 1.

Deformation mechanism in laser-stimulated 4D printing prototypes

To determine the optimal processing parameters for shaping quality, ten different printing parameters were used for forming 3D parts with LPBF technology (Supplementary Fig. 6 and Supplementary Table 2). This experiment utilized a SEM for microstructural characterization of rectangular block samples numbered 1 to 10 (Supplementary Figs. 7–9). To minimize the impact of residual stress on the 3D printed part, a widely used stress relief method was employed. After each layer was processed by the laser, the scanning angle was rotated by 67° before proceeding to the next layer. Dunbar et al. reported that printing with a 67° layer-by-layer rotation reduced deformation by 37.5%³³. This process repeats continuously until the entire 3D component is fully formed. Through analysis, the printing parameters for the LPBF process were selected with the laser power of 175 W, scanning speed of 1200 mm/s, and an inter-layer rotation angle of 67°. The selection of the laser stimulation area and the adjustment of the scanning angle have a significant impact on the 4D printing deformation behavior of Fe-Co-V samples. Based on the analysis of the effect of different laser stimulation parameters on sample deformation as shown in Supplementary Fig. 10, the optimal laser stimulation parameters were selected, as detailed in Supplementary Table 3. The laser power was set to 250 W, and the scanning speed was set to 1600 mm/s. These settings were used as the laser stimulation parameters for subsequent experiments. The laser scanning direction determines the spatial distribution of energy deposition. This defines the orientation of thermal stress. Ultimately, it governs the resulting deformation morphology. When scanning was performed along the length direction, resulting in significant bending deformation (Supplementary Fig. 10). To further explore the effect of laser stimulation on sample deformation, the influence of sample thickness on deformation was investigated. The deformation process of samples with varying thicknesses under laser parameters was analyzed via finite element simulation (Supplementary Fig. 11). Experimental results indicate that increasing sample thickness exerts a suppressing effect on deformation. This is because greater thickness substantially enhances the sample's inherent stiffness, thereby improving its capacity to resist deformation caused by thermal stress. Moreover, thicker samples possess larger heat diffusion areas and exhibit slower temperature changes, thereby diminishing the effect of thermal stresses driving deformation.

Firstly, four conventional geometric 2D precursor patterns were designed in Fig. 2a. These include Fig. 2a, i a square box planar unfolding pattern without a top, Fig. 2a, ii a square quadrangular cone planar unfolding pattern, Fig. 2a, iii an octagonal planar structural pattern, and Fig. 2a, iv a pentagonal planar structural pattern. To validate the feasibility of the laser-stimulated 4D printing deformation method, the planar unfolding pattern of a square tetragonal cone is used as an example. This allows the deformation process to be observed more clearly and intuitively, as illustrated in Fig. 2a, ii. Finite element analysis is performed on the deformation and its process is performed (Supplementary Fig. 12, and Movie 2). Additionally, this investigation achieves functionally oriented gradient bending deformations in four specialized structures, as illustrated in Fig. 2b. The 2D planar pattern depicted in Fig. 2b, i is designed based on a gear structure. And the desired gradient 4D printing deformation is achieved by manipulating the laser scanning directions for the gear teeth. The prototypes shown in Fig. 2b, ii–iv are designed for laser-stimulated 4D printing applications, such as turbine blade structures and shoe sensor devices, targeting specific fields like aerospace, automotive, and electronics. Experimental results demonstrate that by controlling the laser scanning path, the deformation direction can be

preprogrammed. This enables the transformation into graded and complex shapes, such as bending and twisting. The deformation effect of the samples can also be controlled by altering their thickness. Consequently, these facilitate the 4D printing of specific structures.

To visually represent the 4D printing deformation of laser-stimulated magnetostrictive Fe-Co-V materials, the adaptation of natural organisms to their environment was simulated. Biomimetic design principles were applied to mimic the structure and function of natural organisms. The biomimetic deformation includes bending or stretching when stimulated by external environmental factors. Figure 2c presents three different biomimetic structures. These structures simulate the flapping wings of a bat in flight (Fig. 2c, i), the contraction of an eight-petal flower when stimulated (Fig. 2c, ii), and a human hand forming the “I love you” gesture when the middle and ring fingers are stimulated to bend (Fig. 2c, iii). This further validates that by controlling the intensity of laser stimulation and the direction of laser scanning, the amplitude and direction of the biomimetic structure deformation can be controlled. In addition, a blade-like antenna structure (Supplementary Fig. 13) is designed to mimic the inward wrapping motion of a blade under sunlight exposure (Supplementary Movie 3). This design may help filter out excess impurity signals. Furthermore, it efficiently converts electrical signals into electromagnetic waves, enabling long-distance wireless communication. Figure 2d presents three electromagnetic shielding structures developed for electromagnetic applications and ultimately achieves on-demand 4D printing deformation. This approach enabled the realization of gradient-style 4D printing deformation in the electromagnetic shielding structure, as shown in Supplementary Fig. 14. The deformation process was captured in video recordings (Supplementary Movies 4–6).

To provide a more intuitive understanding of the magnetostrictive effect, Fig. 3a illustrates the process of magnetic domain alterations. These alterations occur at the microscopic level when the material experiences magnetostrictive changes. Figure 3b, c depicts the changes in magnetization intensity under varying temperature conditions for the shape-morphing samples during laser stimulation, respectively. In Zero-Field Cooling, a sample is first cooled from high to low temperatures. This cooling process is conducted in the absence of an external magnetic field. Subsequently, the sample is warmed in the presence of a fixed, small magnetic field. During this warming phase, the magnetization is continuously measured. Field-Cooled Cooling refers to a procedure wherein a sample is cooled from high to low temperatures. This cooling occurs under the presence of an external magnetic field. Simultaneously, the magnetization is measured during the cooling process. Field-Cooled Warming involves warming a sample from low to high temperatures. This warming is performed under an applied external magnetic field. The magnetic field intensity is maintained at 100 Oe, and the temperature range is set between 173 and 373 K (equivalent to -100 °C to 100 °C). A comparison of the two sets of magneto-thermal curves reveals that the magnetization intensity of the laser-stimulated samples is higher than that of the LPBF samples. Additionally, the 4D-printed samples exhibit relatively smaller changes in magnetization intensity as the temperature gradually rises. This indicates an enhancement in their ferromagnetic properties. And from the magneto-thermal curves in Fig. 3b, c, it is evident that the changes in magnetization intensity for both the LPBF and 4D-printed samples are relatively minimal. These changes remain consistent despite temperature variation. This demonstrates their strong ferromagnetic properties. Besides, the absence of a Curie point further confirms that the Fe-Co-V is magnetostrictive with high Curie temperatures. The relevant magnetic properties of the Fe-Co-V alloy are presented in Supplementary Table 4. These magnetic materials can sustain their magnetization state at elevated temperatures. And this allows them to preserve strong magnetic properties and minimize magnetic loss.

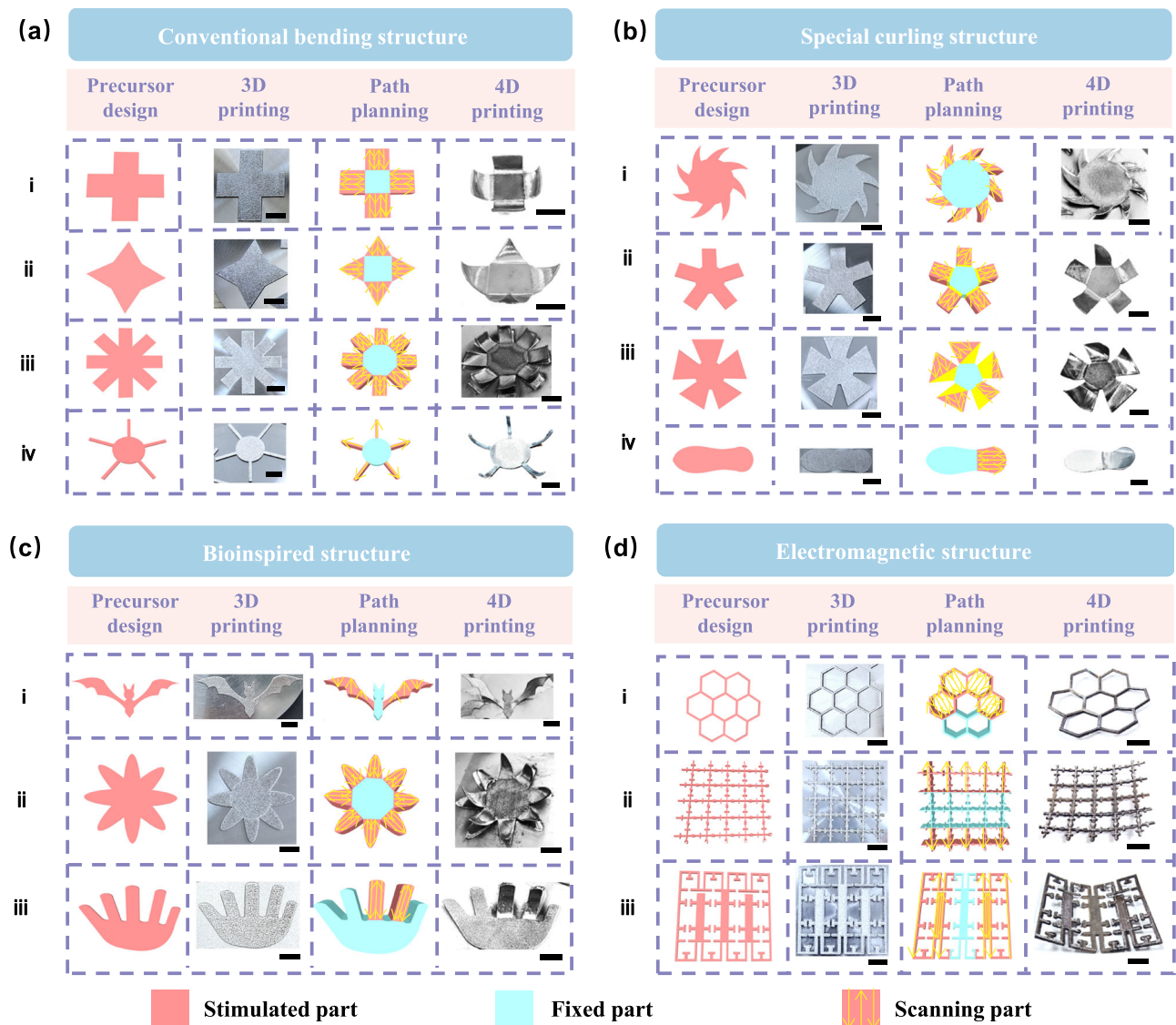


Fig. 2 | Experimental investigation of the shape-morphing processes from 2D to 3D. 4D printing deformation effect of four distinct structural categories. The structures include: **a** four conventional bending structures (i a planar net of an open-top square box; ii a planar net of a square pyramid; iii an octagonal planar structural pattern; iv a pentagonal planar structural pattern), **b** four unique bending

structures (i a gear structure; ii, iii turbine blade structures; iv a shoe sensor device), **c** three types of biomimetic structures (i a bat structure; ii an eight-petalled flower structure; iii a human hand structure), and **d** three types of electromagnetic structures (i-iii three electromagnetic shielding structures). Scale bar: 10 mm.

Consequently, these magnetic materials are appropriate for utilization in high-temperature equipment and environments.

The shape-morphing samples were tested to evaluate the magnetostrictive and basic magnetic properties of Fe-Co-V. Figure 3d shows the magnetostrictive changes along the direction of the magnetic field for the LPBF samples and three sets of 4D-printed samples. Sample 1# is the LPBF sample. Sample 2# is the 4D printed sample with a triangular pattern. Sample 3# corresponds to the 4D printed sample with a rectangular pattern. And sample 4# is the 4D printed sample with a claw-shaped pattern. As shown in Fig. 3d, the blue curve represents the 3D printed samples. These samples exhibit a smaller magnetostrictive strain compared to the other three sets of 4D printed samples. In contrast, the three deformed 4D printed samples, achieved through laser stimulation, all demonstrate greater length change characteristics under a magnetic field. This indicates superior magnetostrictive performance. Based on the images inserted in Fig. 3d, an analysis of Samples 2#–4# was performed. All 4D printed samples,

after laser stimulation, exhibit excellent magnetic field-driven performance. These patterns suggest a higher degree of structural uniformity, which in turn enhances their magnetostrictive performance. In contrast, the surface of 3D printed samples before laser stimulation showed irregular particles or layered structures. As a result, they lead to lower magnetostrictive performance. Specifically, laser stimulation generates residual stress on the surface of the sample. This residual stress influences the orientation and motion of magnetic domains. Such influence is mediated through the magnetoelastic coupling effect. Magnetostriction is typically anisotropic. When there is a difference in cooling rates between the top and bottom surfaces, a gradient in grain orientation or texture strength may be generated. Consequently, the magnetostrictive response will vary spatially. However, from another perspective, this phenomenon offers a unique opportunity. It enables the active design and fabrication of functionally graded 4D-printed smart structures. Such structures can achieve complex and programmable deformations under a uniform external

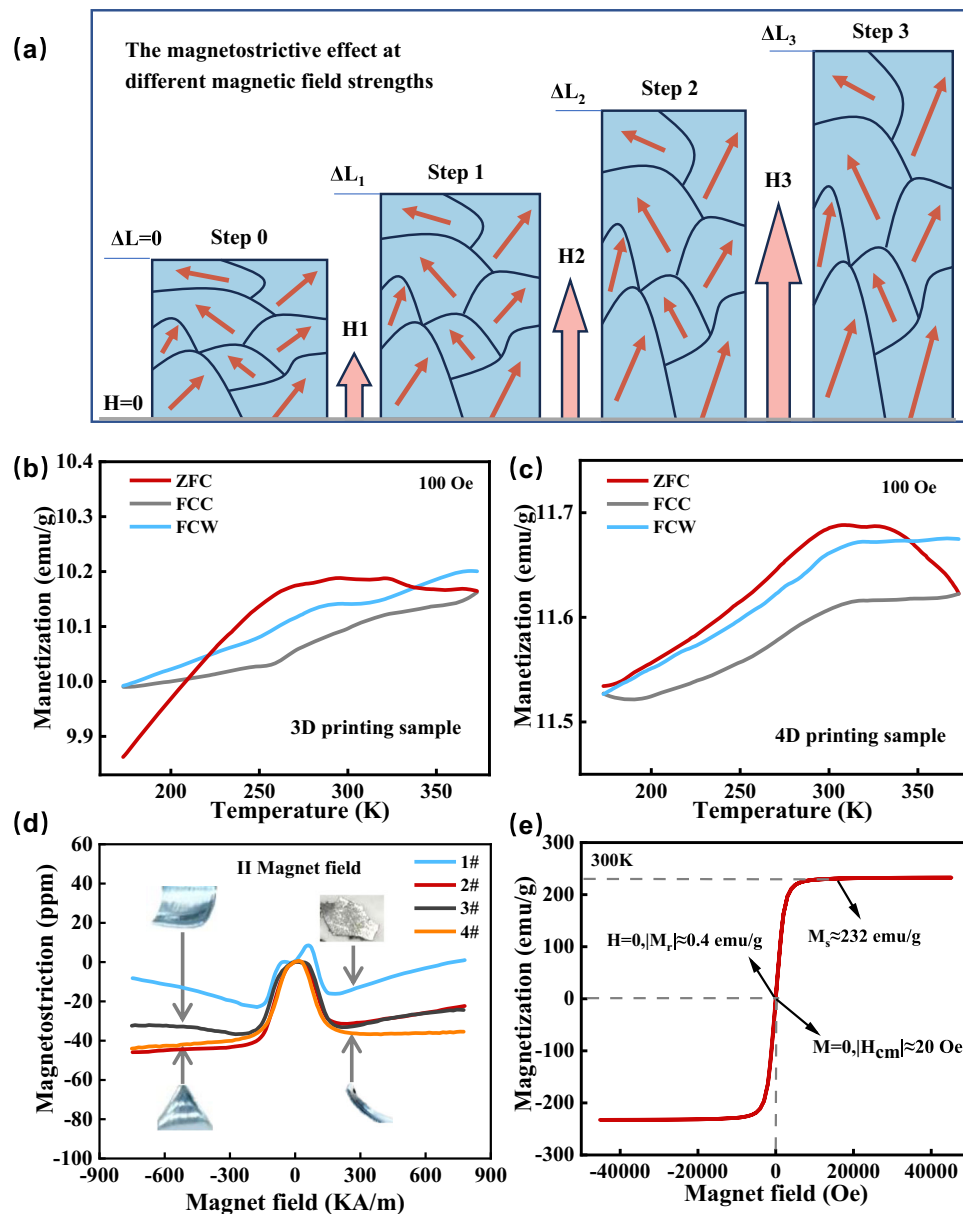


Fig. 3 | The magnetostrictive and basic magnetic properties of shape-morphing samples. **a** Micromechanical interpretation of the magnetostrictive effect at different magnetic field intensities. **b** Magneto-thermal behavior of the LPBF sample. **c** Magneto-thermal behavior of the 4D-printed sample. **d** Magnetostrictive

performance characteristics of the LPBF sample and three 4D-printed samples. **e** Hysteresis loop analysis of the 4D-printed samples. (Source data are provided as a Source Data file).

field. This approach expands the application potential of magnetostrictive materials and 4D printing, including soft robotics, adaptive structures, and novel sensors. Traditional methods often involve embedding new materials or using heat treatment to enhance magnetostrictive performance. In comparison to other investigations on the magnetostrictive properties of Fe-Co alloys³⁴ and Fe-Ga alloys³⁵, this work introduces a approach using metal 4D printing of laser stimulation. This approach not only induces macroscopic deformation but also enhances the magnetostrictive properties of the samples at the microscopic scale. The optimal test specimens achieved a saturation magnetostriction value of 60–70 ppm. This performance is comparable to that of Fe-Co alloys produced by conventional processing routes³⁶. LPBF-based 4D printing enables the direct fabrication of complex structure. Such geometries are difficult to process via the traditional manufacturing techniques. Although Fe-Ga alloys exhibit higher magnetostriction³⁷, Fe-Co-V alloys offer higher saturation

magnetization and superior mechanical strength. Thus, they may be more suitable for certain application scenarios. This investigation provides a pathway for fabricating integrated devices. These devices combine desirable magnetostrictive properties, complex geometries, and high mechanical strength.

The magnetostrictive performance curves of the two 4D-printed samples tested perpendicular to the magnetic field direction were examined. And it is apparent that the claw-shaped 4D-printed sample exhibits a larger magnetostrictive strain. This strain is greater than that of the rectangular 4D-printed sample, as shown in Supplementary Fig. 15. The magnetostrictive strain in the rectangular 4D-printed samples differs from the results in the parallel direction. This suggests that the magnetostrictive properties of these samples are more influenced by the orientation of the applied magnetic field. When the magnetic field is applied perpendicular to the sample surface, the amplitude of magnetic domain rearrangement decreases

considerably. And this decrease is reflected in the macroscopic deformation. As a result, the magnetostrictive strain of the rectangular 4D printed samples in the perpendicular direction is significantly reduced. The hysteresis loops of the laser-stimulated samples at a temperature of 300 K are shown in Fig. 3e. And these loops further demonstrate the material's strong saturation magnetization. When the sample reaches magnetic saturation, the magnetization intensity reaches 232 emu/g. When the magnetic field intensity is reduced to zero, the remaining magnetization of the sample is 0.4 emu/g. This indicates that the material has strong magnetization capabilities and can display excellent magnetic properties under high magnetic fields. Furthermore, when the magnetization is reduced to zero, the coercivity (H_{cm}) is -20 Oe. To determine whether laser stimulation affects the fundamental magnetic properties of the samples, the corresponding magnetic properties were tested. And the hysteresis loops of the LPBF samples showed similar results (Supplementary Fig. 16). It is evident that physical parameters such as coercivity and saturation magnetization strength did not show significant changes before and after laser stimulation. This suggests that the laser stimulation did not alter the material's inherent magnetic properties.

Assessment of electromagnetic shielding effectiveness

Based on electromagnetism theories and testing techniques, the electromagnetic shielding performance of shape-morphing samples during laser stimulation is analyzed. The tests cover both frequency-domain and time-domain performance in three different frequency ranges. This enabled an investigation into how their electromagnetic shielding capabilities are affected. Figure 4a presents the electromagnetic shielding performance of the laser-stimulated samples in the 12–18 GHz frequency range. Shielding effect reflection loss (SER), total shielding effectiveness (SET) and shielding effect absorption loss (SEA) are parameters used to describe electromagnetic shielding performance. These three quantities are related through the equation: $SET = SER + SEA$. The total shielding efficiency exceeds 40 dB, demonstrating strong electromagnetic shielding capabilities. And it effectively absorbs electromagnetic waves within the 12–18 GHz frequency band. To examine the changes in electromagnetic shielding performance of the sample during the processes of laser stimulation, a clearer conclusion can be drawn from the curves shown in Fig. 4b. In the frequency range of 18 to 25 GHz, the SET values of the 3D and 4D printed samples remains relatively similar. However, the SET of the LPBF samples increases sharply over a narrow frequency range when the frequency exceeds 25 GHz. The SET of the electromagnetic shielding material initially exceeds 70 dB, then gradually decreases to 40 dB as the signal frequency increases. Additionally, similar electromagnetic shielding performance curves were tested in the 26.5–40 GHz frequency range, with the results shown in Fig. 4c. As observed in Fig. 4c, the overall shielding performance of the 4D-printed samples is superior to that of the LPBF samples in this frequency range. The SET exceeds 50 dB.

To systematically evaluate the electromagnetic shielding properties, time-domain tests were conducted. These tests focused on the 3D and 4D printed samples within the same three frequency bands. The results of these tests are presented in Fig. 4d–f. The curve in Fig. 4d shows that the SET of the 4D-printed samples is somewhat lower when measured by the time-domain test method in the 12–18 GHz range. This shielding performance is reduced compared to the measurements shown in Fig. 4a. Similarly, the curve of the LPBF samples in the 18–26.5 GHz range shown in Fig. 4e exhibits a trend consistent with the curve of the LPBF sample in Fig. 4b. Comparing the curves of the 4D-printed samples in Fig. 4b, e, it is observed that the time-domain SEA surpasses the frequency-domain SEA only when the frequency reaches 22 GHz. Additionally, the time-domain SER of the 4D-printed samples consistently exceeds the frequency-domain SER throughout the 18–26.5 GHz frequency range. Within the frequency range of

26.5–40 GHz, the SET of the LPBF samples measured using the time-domain method shows consistent results. There is no significant difference compared to the measurements obtained via the frequency-domain method. In both cases, the overall SET of the LPBF samples remains in the range of 20–40 dB. Meanwhile, the SET of the 4D-printed samples measured by the time-domain method shows a slight decrease. This is compared to the SET of the 4D-printed samples measured in the frequency domain.

By comparing the electromagnetic shielding performance curves of the samples before and after laser stimulation, some variations were observed in the 4D printed samples compared to the LPBF samples. Analysis of the causes behind these changes indicates that the shielding performance of the laser-stimulated samples is more sensitive to the changes of microstructure. This is because the tests were conducted at high frequencies. When the laser scans the surface of the sample, the high energy density of the laser beam causes the formation of surface microstructures. These structures alter the surface roughness and affect the electromagnetic shielding performance. Furthermore, during laser stimulation, the high temperatures can lead to oxidation of the metal surface. This results in the formation of a metal oxide layer, which affects the surface conductivity and the overall shielding performance.

In summary, this investigation integrates magnetostrictive materials with 4D printing technology to achieve laser-responsive macroscopic strain and magnetically responsive microscopic strain. Dynamic control of electromagnetic properties at the microscopic level can be accomplished during the macro-deformation of LPBF samples. It also addresses the challenge of strain-scale limitations and expands the prospects of magnetostrictive materials to be applied in high-end equipment. This advancement is expected to drive the adoption of 4D printing in the electromagnetic field.

Methods

Material selection

Fe-Co-V, a magnetostrictive material, was chosen as the base material for the subsequent experiments in this investigation. It is classified as 1J22, which is a metal spherical powder with a particle size ranging from 15 to 45 μm . The material primarily consists of iron, cobalt, vanadium, and other elements, with iron accounting for ~64.7%, making it the most critical component of the 1J22 soft magnetic alloy. The soft magnetic alloy also contains trace elements such as C, Cr, Si, Mn, P, and S. With these additional elements, the alloy's performance can be further improved, enabling it to function effectively across various application scenarios.

3D printing of the samples

In this investigation, LPBF technology was utilized to fabricate 3D samples, with the process carried out using the HBD-80 laser melting equipment (Hanbang Lianhang Laser Technology Co., Ltd, Shanghai, CN). The key technical specifications of this equipment include a maximum laser power of 500 W, a maximum scanning speed of 10,000 mm/s, and a build volume of $\phi 120 \text{ mm} \times 80 \text{ mm}$ for the fabricated samples. Initially, the 3D solid sample is printed by selecting suitable laser power and scanning speed based on insights from experimental investigations (Supplementary Fig. 17). Some of these samples were examined microscopically using a digital microscope (Leica DVM6, Leica Microsystems, GR) to verify the reliability and feasibility of the printing parameters (Supplementary Fig. 18). This ensured a solid foundation for the continuation of experiments.

Microstructural characterization

In this experiment, microstructural surface observations and test analyzes were conducted on both LPBF samples and 4D-printed samples through laser stimulation. Firstly, the 3D solid samples formed by LPBF technology were separated from the substrate using wire cutting

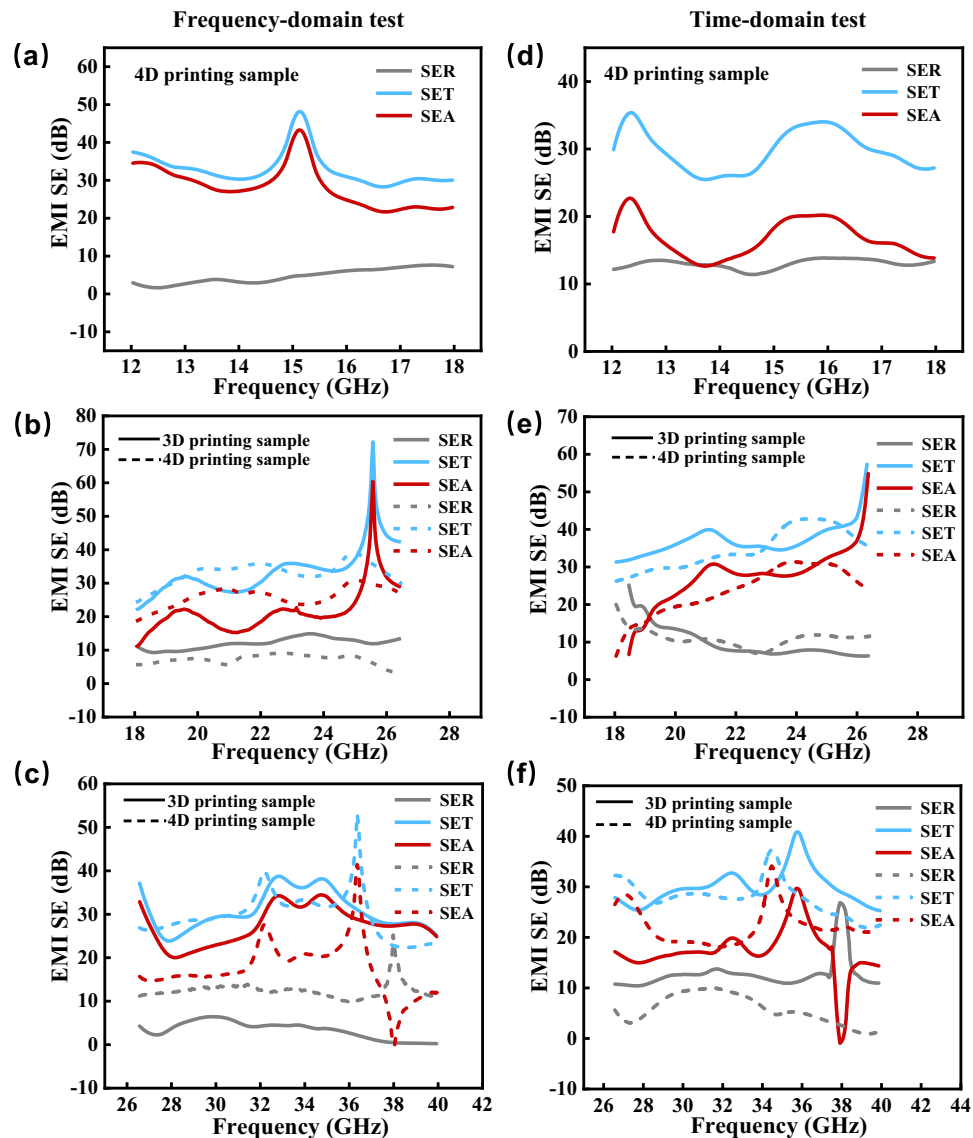


Fig. 4 | The electromagnetic shielding performance for LPBF and 4D-printed samples. **a** Test results for the frequency-domain electromagnetic shielding performance of laser-stimulated samples in the 12 to 18 GHz band. **b** Test results for the frequency-domain electromagnetic shielding performance of laser-stimulated samples in the 18 to 26.5 GHz band. **c** Test results for the frequency-domain electromagnetic shielding performance of laser-stimulated samples in the 26.5 to

40 GHz band. **d** Test results for the time-domain electromagnetic shielding performance of laser-stimulated samples in the 12 to 18 GHz band. **e** Test results for the time-domain electromagnetic shielding performance of laser-stimulated samples in the 18 to 26.5 GHz band. **f** Test results for the time-domain electromagnetic shielding performance of laser-stimulated samples in the 26.5 to 40 GHz band. (Source data are provided as a Source Data file).

technology. The surfaces of the samples were then polished to meet the requirements for material testing. Subsequently, the surface of the 4D-printed sample via the laser stimulation was characterized using a SEM (Zeiss GeminiSEM360/Sigma300, Carl Zeiss AG, GR). Additionally, specific areas were also examined through EDS analysis (Zeiss GeminiSEM360/Sigma300, Carl Zeiss AG, GR) to identify the elemental composition and content ratios on the sample's surface. The primary substances present on the sample's surface were analyzed using XRD (XRD-6100, Shimadzu, JPN). The diffraction angle range was set between 5° and 90° with a scanning speed of $2^\circ/\text{min}$. At last, the composition of the sample was analyzed to identify the primary substances in the sample.

Mechanical properties measurement

The mechanical properties of the deformed samples after laser stimulation were briefly tested. For instance, a rectangular 3D solid sample with surface dimensions of $4\text{ cm} \times 1\text{ cm}$ was exposed to varying

numbers of laser stimulations. Subsequently, compression tests were performed on five groups of deformed samples. These tests examined the variations in compressive properties and plasticity after 2, 4, 8, and 10 laser stimulations.

Magnetic and magnetostriction properties

The basic magnetic and magnetostrictive properties of the LPBF and laser-stimulated samples were evaluated. This was done to investigate the effects of the laser stimulation 4D printing method on the electromagnetic properties of the samples. The magnetic properties of the samples were measured using a superconducting quantum interference device (SQUID, Quantum Design, USA). The measurements were conducted within a temperature range of 1.8 K to 400 K and a magnetic field range of 0 to 50 kOe. Besides, thermal expansion curves of the blocks were obtained using strain gauges on the AC Transport (ACT) module of the physical property measurement system (PPMS, Quantum Design, USA). The sample used for the thermal expansion

curve test measured $2 \times 2 \times 2$ mm. Furthermore, the strain gauges were BA120-05AA-A150 (I1) models (AVIC Electro-Measurement, CN). And the adhesive used to bond the strain gauges to the sample was B711 room-temperature glue (AVIC Electro-Measurement, CN). By measuring the variation in resistance of the strain gauge compared to its initial resistance as the temperature changes, the dimensional change of the sample can be determined. This is achieved by using the sensitivity coefficient conversion to account for the influence on the strain gauge grid. To account for the dimensional changes of the strain gauge itself in a variable temperature environment, a Wheatstone Bridge was employed. This approach eliminated the influence, thereby enhancing the accuracy of the measurement. Related calculations can be found as follows:

$$V_{out} = V_{in} \cdot GF \cdot \varepsilon / 4 \quad (1)$$

Where: V_{out} represents the output voltage of the bridge (in volts), while V_{in} refers to the input voltage of the bridge (in volts). GF denotes the sensitivity factor of the strain gauge, and ε is the strain. In the calculation, ε is substituted according to the strain equation.

$$\varepsilon = 4 \cdot V_{out} / V_{in} \cdot GF \quad (2)$$

Testing of electromagnetic shielding effectiveness

Electromagnetic shielding performance was assessed using a vector network analyzer (8–40 GHz). The scattering parameters, S_{11} and S_{21} of the materials were measured via the waveguide method on a comprehensive electromagnetic material testing platform (CEC Siyi Technology Co, Qingdao, CN). The waveguide calibrators used were 32117 (8–12 GHz), 32118 (12–18 GHz), 32119 (18–26.5 GHz), and 32101 (26.5–40 GHz), corresponding to sample sizes of 22.86×10.16 mm, 15.80×7.90 mm, 10.67×4.32 mm, and 7.12×3.56 mm, respectively. For the electromagnetic shielding effectiveness (SE), the calculation formula is described as follows:

$$R = |S_{11}|^2 \quad (3)$$

$$T = |S_{21}|^2 \quad (4)$$

$$SE_R = -10 \log(1 - R) \quad (5)$$

$$SE_A = -10 \log(T / (1 - R)) \quad (6)$$

The SE_T is determined by:

$$SE_T = SE_R + SE_A \quad (7)$$

Software utilized

The finite element simulations in Supplementary Figs. 11 and 12 were done with Abaqus 2020. The stimulation parameters were maintained consistent with the actual parameters. The Gaussian heat source model was employed to simulate the laser. The model was built based on the actual sample size and shape. Additionally, boundary conditions were set based on the experimental fixation conditions, and convective heat transfer constraints were appropriately defined. These measures were intended to better simulate the deformation process of the sample under laser stimulation. All other data analysis and charting were performed using Origin 2021.

Data availability

The authors declare that the data supporting the findings of this study are available within this article, Supplementary Information, and the Source Data file provided with this paper. All data are available from the corresponding author upon request. Source data are provided with this paper.

References

- Hu, Q.-M. & Yang, R. The endless search for better alloys. *Science* **378**, 26–27 (2022).
- Joy, B., Cai, Y., Bono, D. C. & Sarkar, D. Cell Rover—a miniaturized magnetostrictive antenna for wireless operation inside living cells. *Nat. Commun.* **13**, 5210 (2022).
- Ito, M. Development of a simple resonance frequency tuning method for magnetostrictive vibration energy harvesters. *J. Magn. Magn. Mater.* **552**, 169211 (2022).
- Norhaniza, R. et al. Enhancement of sensitivity of magnetostrictive foam in low magnetic fields for sensor applications. *Polymer* **211**, 123083 (2020).
- Yamaura, S., Nakajima, T., Kamata, Y., Sasaki, T. & Sekiguchi, T. Production of vibration energy harvester with impact-sliding structure using magnetostrictive Fe-Co-V alloy rod. *J. Magn. Magn. Mater.* **514**, 167260 (2020).
- Li, Y., Huang, W. & Wang, B. Design and output characteristics of ultrasonic transducer based on rare-earth giant magnetostrictive material. *IEEE Trans. Magn.* **58**, 1–6 (2022).
- Suman, S. D., Hirwani, C. K., Chaturvedi, A. & Panda, S. K. Effect of magnetostrictive material layer on the stress and deformation behaviour of laminated structure. *IOP Conf. Ser. Mater. Sci. Eng.* **178**, 012026 (2017).
- Huang, W., Gao, C., Li, Y. & Wang, B. Experimental and calculating analysis of high-frequency magnetic energy losses for terfenol-D magnetostrictive material. *IEEE Trans. Magn.* **54**, 1–4 (2018).
- Lin, H. et al. Fabrication of magnetostrictive composites using metallic glass as glue. *Intermetallics* **145**, 107561 (2022).
- Huang, W., Xia, Z., Guo, P. & Weng, L. Analysis and experimental research on high frequency magnetic properties of different magnetostrictive materials under variable temperature conditions. *AIP Adv.* **12**, 035231 (2022).
- Zhang, Y. et al. Depth-dependent decomposition and property of large magnetostriction Fe-Ga alloys. *Appl. Surf. Sci.* **569**, 151059 (2021).
- Gao, C., Zeng, Z., Peng, S. & Shuai, C. Magnetostrictive bulk Fe-Ga alloys prepared by selective laser melting for biodegradable implant applications. *Mater. Des.* **220**, 110861 (2022).
- Wei, Y. et al. Ultralow magnetic damping of a common metallic ferromagnetic film. *Sci. Adv.* **7**, eabc5053 (2021).
- Shi, P. One-dimensional magneto-mechanical model for anhyseretic magnetization and magnetostriction in ferromagnetic materials. *J. Magn. Magn. Mater.* **537**, 168212 (2021).
- Nakajima, K., Kurita, H. & Narita, F. Performance boost of co-rich Fe-Co based alloy magnetostrictive sensors via nitrogen treatment. *Sens. Actuators A Phys.* **295**, 75–83 (2019).
- Liang, J. et al. CO₂ hydrogenation over Fe-Co bimetallic catalysts with tunable selectivity through a graphene fencing approach. *Nat. Commun.* **15**, 512 (2024).
- Marczewski, M. et al. Microstructure and mechanical properties of Ti-Nb alloys: comparing conventional powder metallurgy, mechanical alloying, and high power impulse magnetron sputtering processes for supporting materials screening. *J. Mater. Sci.* **59**, 9107–9125 (2024).
- Zhang, W., Zhang, W., Jiang, H., Peng, B. & Yang, S. Preparation and characterization of thick magnetostrictive films. *J. Magn. Magn. Mater.* **261**, 118–121 (2003).

19. Yao, X. et al. Magnetostrictive strain-sensitivity synergy for laser-beam powder bed fusion processed Fe₈₁Ga₁₉ alloys by magnetic field annealing. *Adv. Powder Mater.* **3**, 100216 (2024).
20. Gao, C., Wang, L., Deng, Y., Peng, S. & Shuai, C. Multifactorial impacts of B-doping on Fe₈₁Ga₁₉ alloys prepared by laser-beam powder bed fusion: microstructure, magnetostriction, and osteogenesis. *J. Mater. Sci. Technol.* **205**, 14–26 (2025).
21. Zhang, Q. et al. Laser-induced in situ reprogramming of magnetic shape memory composites for adaptive devices. *Int. J. Extreme Manuf.* **8**, 015508 (2026).
22. Ozden, M. G. & Morley, N. A. Laser additive manufacturing of Fe-based magnetic amorphous alloys. *Magnetochemistry* **7**, 20 (2021).
23. Chen, H. et al. Microstructure and mechanical properties of additive manufactured W-Ni-Fe-Co composite produced by selective laser melting. *Int. J. Refractory Met. Hard Mater.* **86**, 105111 (2020).
24. Gao, C., Yao, X., Deng, Y., Pan, H. & Shuai, C. Laser-beam powder bed fusion followed by annealing with stress: a promising route for magnetostrictive improvement of polycrystalline Fe₈₁Ga₁₉ alloys. *Addit. Manuf.* **68**, 103516 (2023).
25. Riipinen, T. et al. Properties of soft magnetic Fe-Co-V alloy produced by laser powder bed fusion. *RPJ* **25**, 699–707 (2019).
26. Riipinen, T. et al. The effect of heat treatment on structure and magnetic properties of additively manufactured Fe-Co-V alloys. *Mater. Today Commun.* **36**, 106437 (2023).
27. Feng, P. et al. Mechanism and manufacturing of 4D printing: derived and beyond the combination of 3D printing and shape memory material. *Int. J. Extrem Manuf.* **6**, 062011 (2024).
28. Inoue, S. et al. High-performance vibration power generation using polycrystalline Fe-Co-based alloy due to large inverse magnetostrictive effect. *AIP Adv.* **11**, 035021 (2021).
29. Wang, L., Zhang, H., Hu, A., Li, Y. & Pei, R. Research on torque performance of a traction motor by using Fe-Co-V soft magnetic alloys. *IEEE Trans. Magn.* **58**, 1–6 (2022).
30. Zhang, Y. & Gu, J. A Perspective for developing polymer-based electromagnetic interference shielding composites. *Nano-Micro Lett.* **14**, 89 (2022).
31. Zheng, X., Zhang, H., Liu, Z., Jiang, R. & Zhou, X. Functional composite electromagnetic shielding materials for aerospace, electronics and wearable fields. *Mater. Today Commun.* **33**, 104498 (2022).
32. Liu, G. et al. Research on the effect of remelting on the epitaxial growth process of single crystal superalloy. *J. Mater. Res. Technol.* **31**, 888–897 (2024).
33. Dunbar, A. J. et al. Development of experimental method for in situ distortion and temperature measurements during the laser powder bed fusion additive manufacturing process. *Addit. Manuf.* **12**, 25–30 (2016).
34. Komagome, R., Katabira, K., Kurita, H. & Narita, F. Characteristics of carbon fiber reinforced polymers embedded with magnetostrictive Fe-Co wires at room and high temperatures. *Compos. Sci. Technol.* **228**, 109644 (2022).
35. Gao, C., Zeng, Q., Deng, Y., Peng, S. & Shuai, C. Synergistic effects of laser powder bed fusion and annealing on the texture-selective recrystallization of magnetostrictive Fe-Ga-NbC alloys for biomedical applications. *J. Adv. Res.* **69**, 565–580 (2025).
36. Kurita, H., Lohmuller, P., Laheurte, P., Nakajima, K. & Narita, F. Additive manufacturing and energy-harvesting performance of honeycomb-structured magnetostrictive Fe₅₂-Co₄₈ alloys. *Addit. Manuf.* **54**, 102741 (2022).
37. Gou, J. et al. Large and sensitive magnetostriction in ferromagnetic composites with nanodispersive precipitates. *NPG Asia Mater.* **13**, 6 (2021).

Acknowledgements

This study is supported by the National Natural Science Foundation of China (Grant No. 52105342, G.L.), Jilin Province Key Research and Development Project (20240302046GX, G.L.), and Young Elite Scientists Sponsorship Program by CAST (2023QNRC001, G.L.).

Author contributions

G.W.L., Z.Y.Y., and Q.L. analyzed the data and wrote the paper. G.W.L. provided the methodology. Z.Y.Y. carried out the simulation work. A.D.Z. and Q.T. analyzed the characterization results. W.Z.W. and X.W. revised the paper. All the authors contributed to the discussions on the results.

Competing interests

The authors declare no competing interests.

Additional information

Supplementary information The online version contains supplementary material available at <https://doi.org/10.1038/s41467-026-69378-0>.

Correspondence and requests for materials should be addressed to Guiwei Li, Qi Li, Xin Wang or Wenzheng Wu.

Peer review information *Nature Communications* thanks the anonymous reviewers for their contribution to the peer review of this work. A peer review file is available.

Reprints and permissions information is available at <http://www.nature.com/reprints>

Publisher's note Springer Nature remains neutral with regard to jurisdictional claims in published maps and institutional affiliations.

Open Access This article is licensed under a Creative Commons Attribution-NonCommercial-NoDerivatives 4.0 International License, which permits any non-commercial use, sharing, distribution and reproduction in any medium or format, as long as you give appropriate credit to the original author(s) and the source, provide a link to the Creative Commons licence, and indicate if you modified the licensed material. You do not have permission under this licence to share adapted material derived from this article or parts of it. The images or other third party material in this article are included in the article's Creative Commons licence, unless indicated otherwise in a credit line to the material. If material is not included in the article's Creative Commons licence and your intended use is not permitted by statutory regulation or exceeds the permitted use, you will need to obtain permission directly from the copyright holder. To view a copy of this licence, visit <http://creativecommons.org/licenses/by-nc-nd/4.0/>.

© The Author(s) 2026